# Micromagnetic modeling of terahertz oscillations in an antiferromagnetic material driven by the spin Hall effect

V. Puliafito,[1] R. Khymyn,[2] M. Carpentieri,[3] B. Azzerboni,[1] V. Tiberkevich,[4] A. Slavin,[4] and G. Finocchio[5]

[1]*Department of Engineering, University of Messina, 98166 Messina, Italy*
[2]*Department of Physics, Gothenburg University, 40530 Gothenburg, Sweden*
[3]*Department of Electrical and Information Engineering, Politecnico of Bari, 70125 Bari, Italy*
[4]*Department of Physics, Oakland University, Rochester, Michigan 48309, USA*
[5]*Department of Mathematical and Computer Sciences, Physical Sciences and Earth Sciences, University of Messina, 98166 Messina, Italy*

The realization of terahertz (THz) sources is a fundamental aspect for a wide range of applications. Over different approaches, compact THz oscillators can be realized, taking advantage of dynamics in antiferromagnetic thin films driven by the spin Hall effect. Here we perform a systematic study of these THz oscillators within a full micromagnetic solver based on the numerical solution of two coupled Landau-Lifshitz-Gilbert-Slonczewski equations, considering ultrathin films. We find two different dynamical modes depending on the strength of the Dzyaloshinskii-Moriya interaction (DMI). At low DMI, a large-amplitude precession is excited, where both the magnetizations of the sublattices are in a uniform state and rotate in the same direction. At large enough DMI, the ground state of the antiferromagnet becomes nonuniform and the antiferromagnetic dynamics is characterized by ultrafast domain-wall motion.

## I. INTRODUCTION

Terahertz (THz) radiation covers the range of frequencies from 300 GHz (gigahertz) to 3 THz, between microwaves and infrared, corresponding to wavelengths ranging from 1000 to 100 $\mu$m [1,2]. Since a wide variety of lightweight molecules emits in this range of the electromagnetic spectrum, THz were intensely investigated by astronomers and chemists in the past [3,4]. However, THz oscillations have turned out to be very promising in many other fields, such as biomedicine [5], defense and security [6], material science [7], industrial nondestructive testing [8], and information and communication technology [9,10]. THz sources can be realized with quantum cascade lasers [11] and solid-state devices [12]; however, the development of compact nanosized electrical generators and receivers of THz signals represents a key challenge of the modern technology. With the experience matured after decades of research on the generation and manipulation of GHz-frequency dynamics in ferromagnetic materials [13–18], the development of high-quality antiferromagnetic materials (AFMs) for several applications [19–23], and proof of concept of antiferromagnetic memories [24–27] driven by the spin Hall effect (SHE) [28], research is now combining this know-how focusing on the development of AFM-based oscillators for application in 4G and 5G telecommunication systems [29–35]. Up to now, there is no experimental proof of AFM-based oscillators, and all the theoretical studies are considering two sublattices with their magnetizations antiferromagnetically coupled [36] and their dynamics is studied by solving two Landau-Lifshitz-Gilbert-Slonczewski equations [37] within the macrospin approximation [29,31,32].

The first motivation of this work is to extend the study of AFMs to a full micromagnetic framework for considering possible nonuniformities of the magnetization. Second, we want to move a step forward to the understanding of THz AFM dynamics driven by a dampinglike torque originating from the spin Hall effect in a typical bilayer AFM heavy metal. We focus, in particular, on 1–5-nm-thick film of nickel oxide and, although we assume a small exchange stiffness constant as compared to the bulk values, THz dynamics can be excited at large enough current. We show a systematic study of the threshold currents and the output frequency as a function of spin-polarization direction, exchange constant, Gilbert damping, AFM thickness, and Dzyaloshinskii-Moriya interaction (DMI) coming from the interface between the AFM and the heavy metal [38].

We find that the DMI is the most influent parameter in controlling the type of AFM dynamics. At low DMI, the threshold current is a subcritical Hopf bifurcation [39] and the dynamics is related to a large-amplitude uniform precession of the magnetization of the two sublattices in the same direction with an angle between the magnetization and the precession axis that depends on the applied current. As the DMI increases, the ground state becomes nonuniform and the excited dynamics changes qualitatively since it is related to a continuous domain-wall nucleation, propagation, and annihilation. In addition, the threshold current is a supercritical Hopf bifurcation. Our results highlight that a full micromagnetic model can be used for the description of all the scenarios where AFM oscillations occur.

This paper is organized as follows. Section II is devoted to the micromagnetic model developed for the analysis. Results
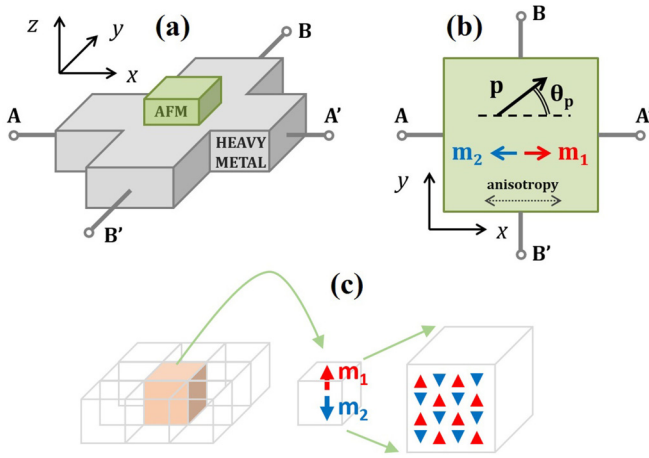
FIG. 1. Schemes of the device under investigation with the indication of the Cartesian reference systems. (a) A schematic of the bilayered ASHO. The four terminals can be used for the application of charge currents, and for the measurement of the spin Hall resistance. (b) Top view of the antiferromagnet. $\mathbf{m}_1$ and $\mathbf{m}_2$ represent the initial configuration of the magnetizations of the two sublattices while $\mathbf{p}$ is the spin polarization. (c) Sketch of the idea at the basis of the continuous modeling of antiferromagnetic sublattices. For a given computational cell we consider that the average magnetization is given by the two vectors $\mathbf{m}_1$ and $\mathbf{m}_2$.

are given in Sec. III in detailed paragraphs, then the conclusions are summarized in Sec. IV.

## II. MODEL

The device under examination is an AFM-based spin Hall oscillator (ASHO), consisting of an antiferromagnetic layer coupled to a four-terminal heavy metal layer, representing both electrodes and source of spin current [32] [see Figs. 1(a) and 1(b), where the Cartesian coordinate systems are also shown]. The AFM has a square cross section with dimensions $40 \times 40\,\text{nm}^2$, whereas the thickness $d$ varies from 1 to 5 nm. We use a continuous micromagnetic formalism, which extends the one of ferromagnets, considering the macroscopic properties of an AFM as computed from averaging the spin vectors [40]. In detail, starting from the atomistic model, the magnetization at each point is modeled by means of two vectors $\mathbf{m}_1$ and $\mathbf{m}_2$ [Fig. 1(c)] that are the average magnetic effect of the spins pointing parallel or antiparallel to a specific direction. AFM dynamics of $\mathbf{m}_1$ and $\mathbf{m}_2$ is obtained by solving two coupled Landau-Lifshitz-Gilbert equations, where the SHE-driven spin transfer torque is taken into account by means of an additional Slonczewski-like torque term [36]:

$$
\begin{aligned}
\frac{d\mathbf{m}_1}{d\tau} &= -(\mathbf{m}_1 \times \mathbf{h}_{\text{eff-1}}) + \alpha \mathbf{m}_1 \times \frac{d\mathbf{m}_1}{d\tau} + d_J(\mathbf{m}_1 \times \mathbf{m}_1 \times \mathbf{p}) \\
\frac{d\mathbf{m}_2}{d\tau} &= -(\mathbf{m}_2 \times \mathbf{h}_{\text{eff-2}}) + \alpha \mathbf{m}_2 \times \frac{d\mathbf{m}_2}{d\tau} + d_J(\mathbf{m}_2 \times \mathbf{m}_2 \times \mathbf{p})
\end{aligned}
$$

$$(1)$$

On the left-hand side of Eq. (1), $\mathbf{m}_1$ and $\mathbf{m}_2$ are therefore the magnetizations of the two sublattices, normalized with respect to the saturation magnetization $M_S$, and $\tau$ is the

dimensionless time $\tau = \gamma_0 M_S t$, where $\gamma_0$ is the gyromagnetic ratio [41]. On the right-hand side, $\mathbf{h}_{\text{eff-1}}$ and $\mathbf{h}_{\text{eff-2}}$ are the normalized effective fields acting on the two sublattices, and $\alpha$ is the Gilbert damping. The third term represents the SHE-driven torque, where $d_J = \frac{g\mu_B J_S}{2\gamma_0 e M_S^2 d}$, $g$ is the Landé factor, $\mu_B$ is the Bohr magneton, $e$ is the electron charge, $J_S$ is the spin current, which is proportional to the charge current $J$ through the so-called spin Hall angle $\theta_{SH}$, $J_S = \theta_{SH} J$. The spin Hall effect creates a Néel torque that is assumed to have the same form for each magnetic sublattice. The vector $\mathbf{p}$ is the direction of the spin Hall polarization, given by $\mathbf{p} = \hat{z} \times \mathbf{j}$, where $\hat{z}$ and $\mathbf{j}$ are the directions of the spin and electric currents, respectively. By a proper combination of the current at the source terminals, it is possible to manage the direction of the spin Hall polarization. In our case, $\mathbf{p}$ can be fixed in the $x - y$ plane with an angle $\theta_{\mathbf{p}}$ between $0°$ and $90°$: If the electric current is applied only at the terminals B-B' (A-A'), then $\theta_{\mathbf{p}} = 0°(\theta_{\mathbf{p}} = 90°)$, resulting in a polarization collinear (normal) to the easy axis; see Fig. 1(b).

The effective fields include the standard contributions from exchange, anisotropy, and demagnetizing field, together with the interfacial DMI and the thermal field:

$$
\begin{aligned}
\mathbf{h}_{\text{eff-1}} &= \mathbf{h}_{\text{exch-1}} + \mathbf{h}_{\text{ani-1}} + \mathbf{h}_{\text{demag-1}} + \mathbf{h}_{\text{dmi-1}} + \mathbf{h}_{\text{th-1}} \\
\mathbf{h}_{\text{eff-2}} &= \mathbf{h}_{\text{exch-2}} + \mathbf{h}_{\text{ani-2}} + \mathbf{h}_{\text{demag-2}} + \mathbf{h}_{\text{dmi-2}} + \mathbf{h}_{\text{th-2}}
\end{aligned}
$$

$$(2)$$

The exchange fields take into account both ferromagnetic coupling between neighbors in each sublattice (this is the same as in the standard model for the ferromagnets) and the antiferromagnetic coupling between the two sublattices. The latter is considered of atomistic origin because the two magnetization vectors are at the same point and it is modeled considering only the homogeneous part,

$$
\begin{aligned}
\mathbf{h}_{\text{exch-1}} &= \alpha_{\text{exch-FM}} \nabla^2 \mathbf{m}_1 + \lambda_{\text{AFM}} \mathbf{m}_2 \\
\mathbf{h}_{\text{exch-2}} &= \alpha_{\text{exch-FM}} \nabla^2 \mathbf{m}_2 + \lambda_{\text{AFM}} \mathbf{m}_1
\end{aligned}
$$

$$(3)$$

where $\alpha_{\text{exch-FM}} = 2A_{\text{FM}}/\mu_0 M_S^2$ and $\lambda_{\text{AFM}} = 4A_{\text{AFM}}/\mu_0 a^2 M_S^2$ ponder the two main contributions, $A_{\text{FM}}$ and $A_{\text{AFM}}$ are the ferromagnetic and antiferromagnetic exchange constant, respectively, $a$ is the lattice constant, and $\mu_0$ is the vacuum permeability.

We consider anisotropy fields originating from uniaxial material:

$$
\begin{aligned}
\mathbf{h}_{\text{ani-1}} &= \alpha_{\text{ani}} \mathbf{m}_1 \cdot \mathbf{u}_k \\
\mathbf{h}_{\text{ani-2}} &= \alpha_{\text{ani}} \mathbf{m}_2 \cdot \mathbf{u}_k
\end{aligned}
$$

$$(4)$$

where $\alpha_{\text{ani}} = 2K_U/\mu_0 M_S^2$, $K_U$ is the uniaxial anisotropy constant, and $\mathbf{u}_K$ is the direction of the easy axis that is the $x$ axis in our study [42].

The demagnetizing field is calculated by solving the magnetostatic problem for the total magnetization $(\mathbf{m}_1 + \mathbf{m}_2)/2$. We have included this field in our simulations because from the theory a small, but not zero, total magnetization is expected. However, some simulations performed without this term of the effective field have provided the same qualitative results with a slight quantitative difference.

The additional contribution to the effective field for considering the interfacial DMI is given by the following

expression:

$$
\begin{aligned}
\mathbf{h}_{\text{dmi-1}} &= -\frac{2D}{\mu_0 M_S}[(\nabla \cdot \mathbf{m}_1)\hat{z} - \nabla m_{z-1}] \\
\mathbf{h}_{\text{dmi-2}} &= -\frac{2D}{\mu_0 M_S}[(\nabla \cdot \mathbf{m}_2)\hat{z} - \nabla m_{z-2}]
\end{aligned}
\tag{5}
$$

with $D$ being the parameter accounting for the intensity of DMI. The boundary conditions now hold, $\frac{d\mathbf{m}_i}{dn} = \frac{1}{\chi}(\hat{z} \times \mathbf{n}) \times \mathbf{m}_i$ $(i = 1, 2)$, where $\mathbf{n}$ is the unit vector perpendicular to the edge and $\chi = \frac{2A_{\text{FM}}}{D}$ is a characteristic length in the presence of DMI.

The thermal field is considered as a stochastic contribution added to the deterministic effective field:

$$
\begin{bmatrix} \mathbf{h}_{\text{th-1}} \\ \mathbf{h}_{\text{th-2}} \end{bmatrix} = \frac{\boldsymbol{\xi}}{M_S}\sqrt{\frac{2\alpha k_B T}{\mu_0 \gamma_0 \Delta V M_S \Delta t}},
\tag{6}
$$

where $k_B$ is the Boltzmann constant, $\Delta V$ and $\Delta t$ are the discretization volume and integration time step, respectively, while $T$ is the temperature. $\boldsymbol{\xi}$ is a six-dimensional white Gaussian noise with zero mean and unit variance, uncorrelated for each computational cell [43,44].

As we are interested in the dynamics of ultrathin antiferromagnetic films, we assume here a substantially low value of the homogeneous intersublattice exchange $A_{\text{AFM}}/a^2 = 1.25 \, \text{MJ/m}^3$, where $a = 0.5$ nm. The discretization cell used for the simulations is 2 nm $\times 2$ nm $\times d$. When not specified, we have used the following parameters for the ASHO: $d = 5$nm, $M_S = 350 \times 10^3 \text{A/m}$, $\alpha = 0.05$, $K_U = 10^5 \text{J/m}^3$, $\theta_{\text{SH}} = 0.2$, and $A_{\text{FM}} = 0.5 \times 10^{-11}$ J/m.

## III. RESULTS

### A. Role of spin-polarization direction

We consider three experimental realizable spin-polarization directions $\mathbf{p}_1$, $\mathbf{p}_2$, and $\mathbf{p}_3$:

(1) $\mathbf{p}_1$ is obtained if the current is applied at the terminals B-B′ along the $-y$ direction $\theta_{\mathbf{p}} = 0°$, the spin polarization is collinear with the equilibrium magnetization of the two sublattices [30];

(2) $\mathbf{p}_2$ is obtained if the same current is applied simultaneously at both A-A′ and B-B′, $\theta_{\mathbf{p}} = 45°$ in the region where the AFM is positioned;

(3) $\mathbf{p}_3$ is obtained if the electric current is applied at the terminals A-A′ along the $x$ direction; hence $\theta_{\mathbf{p}} = 90°$ and the spin polarization is perpendicular to the equilibrium magnetization of the two sublattices [32].

Figures 2(a) and 2(b) show the threshold currents and the oscillation frequencies as a function of current density for the three different spin polarizations without DMI. In all the cases, the self-oscillation is a subcritical Hopf bifurcation characterized by hysteresis with $J_{\text{ON}}$ and $J_{\text{OFF}}$ switching-on and switching-off current densities, respectively. This hysteretic excitation has been already predicted by an analytical theory for the $\mathbf{p}_3$ configuration [32] and can be understood qualitatively by considering that at $J_{\text{ON}}$ the precession of the magnetization of the two sublattices has a finite large amplitude. Differently from subcritical Hopf bifurcation in ferromagnet-based spin transfer torque oscillators [17,45–47], here also at $J_{\text{OFF}}$ the amplitude of the oscillation of sublattices
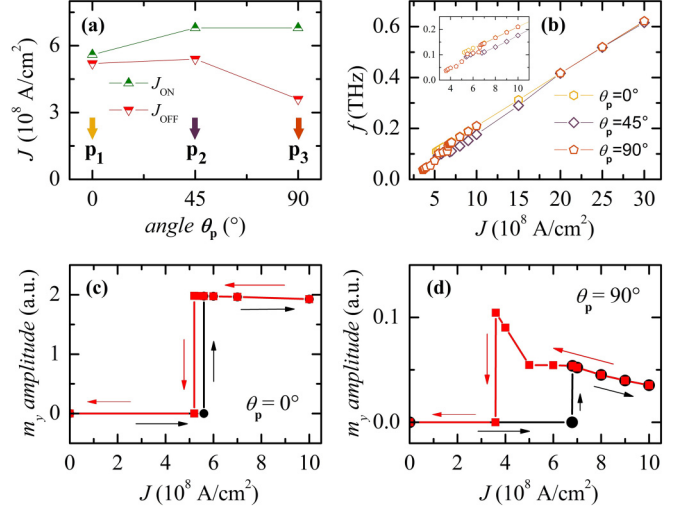


FIG. 2. (a) Threshold current densities ($J_{\text{ON}}$ and $J_{\text{OFF}}$) for the excitation of the antiferromagnetic dynamics for three different directions of spin polarization. (b) Oscillation frequency as a function of the applied current with a zoom near the threshold current. (c), (d) Amplitude of the $y$ component of the magnetization as a function of the current density for $\theta_{\mathbf{p}} = 0°$ and $\theta_{\mathbf{p}} = 90°$.

magnetization is finite and even larger than the one at $J_{\text{ON}}$ [see Figs. 2(c) and 2(d), where the amplitude of the $y$ component of the magnetization for $\theta_{\mathbf{p}} = 0°$ and $90°$ as a function of current density is displayed—-see also Supplemental Material, Note 1 [48], where the differences between subcritical and supercritical Hopf bifurcation for AFMs and FMs are highlighted]. This result is relevant from a technological point of view because the AFM-based oscillator can also work at a current density below $J_{\text{ON}}$ as already pointed out in Ref. [32]. The width of the hysteretic region depends on the polarization direction as for $\theta_{\mathbf{p}} = 0°$ it is very narrow ($0.4 \times 10^8 \text{A/cm}^2$), whereas it increases with the increase of $\theta_{\mathbf{p}}$ ($3.2 \times 10^8 \text{A/cm}^2$ for $\theta_{\mathbf{p}} = 90°$). This result can be directly linked to the fact that the precession axis is parallel to the spin polarization, then at $\theta_{\mathbf{p}} = 0°$ it coincides with the equilibrium axis, while at $\theta_{\mathbf{p}} = 90°$ the precession axis is perpendicular to it (see top right inset of Fig. 3).

The AFM magnetization dynamics is characterized by the rotation of the magnetization of both sublattices $\mathbf{m}_1$ and $\mathbf{m}_2$ in the same direction with an angle $\psi$ with respect to the oscillation axis (top left inset of Fig. 3). The rotation frequency [Fig. 2(b)] exhibits blueshift tunability [21 GHz/($10^8 \text{A/cm}^2$)] and is basically independent of the spin-polarization direction at high currents, which is associated with the high energy of the rotation of the Néel vector, defined as $(\mathbf{m}_1 - \mathbf{m}_2)/2$. The anisotropy of the AFM defines the potential profile for the magnetizations $\mathbf{m}_1$ and $\mathbf{m}_2$ and, thus, the ground state of the AFM. However, at high currents, the kinetic energy of the magnetizations rotation significantly exceeds the potential energy of anisotropy [32], and consequently the angular velocity does not depend on the anisotropy profile and direction of spin polarization. In this case, the frequency is defined only by the spin torque to damping ratio [32]. For a fixed current density, the trajectory is characterized by the same $\psi$ around the oscillation axis fixed by the spin-polarization
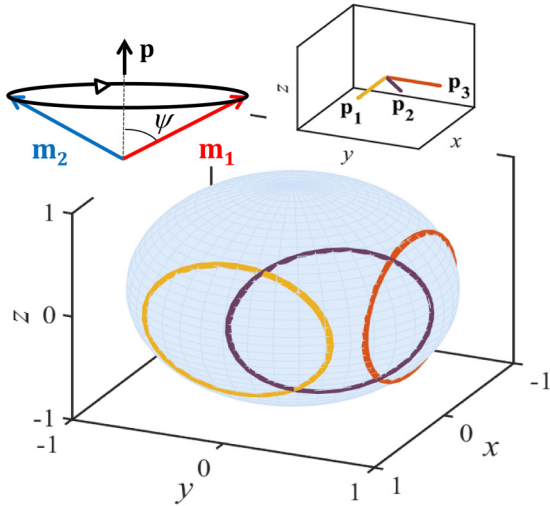
FIG. 3. Trajectories of the magnetizations of the two sublattices in the three different cases of spin Hall polarization, around its direction, for $J = 30 \times 10^8 \mathrm{A/cm^2}$. Left inset: sketch of the precession of the two magnetizations around the spin polarization. Right inset: directions of the spin polarization in the three cases.

direction. This fact is preserved also at very large current; see for example the main panel of Fig. 3 for the trajectories at $J = 30 \times 10^8 \mathrm{A/cm^2}$. As expected from analytical computations the frequency is proportional to the current density (see Eq. (7) of Ref. [32]). For the simulation parameters of this study, a maximum frequency of 0.6 THz at $J = 30 \times 10^8 \mathrm{A/cm^2}$ is observed.

At $\theta_{\mathbf{p}} = 90°$, we have performed a comparison with the analytical model developed in Ref. [32], finding an agreement described below in the paper (see also Supplemental Material, Note 2 [48]).

## B. Output signal

The first challenge to face is the conversion of the AFM dynamics in a measurable THz signal. Some proposed strategies are based on the inverse spin Hall effect [32] or dipolar radiation [49]. Those two approaches need tilting of the magnetization of the two sublattices for originating a net rotating magnetic vector or a time-varying phase angle between the two sublattices; however, for realistic parameters the output power should be very small. On the other hand, our four-terminal scheme can be used biasing the device with a proper current in order to have $\mathbf{p}_1$, $\mathbf{p}_2$, and $\mathbf{p}_3$, and reading the magnetoresistance at one of the couples of terminals AA′ or BB′ [50,51]. For example, when the bias current is applied through the AA′ terminals and hence the spin polarization is $\mathbf{p}_3$, the THz signal should be read out via the BB′ terminals and it is mainly originated by the oscillation of the $y$ component of the magnetization of the two sublattices; such an oscillation has a frequency that is two times the precession frequency (see Supplemental Material, Note 3 [48]). Alternatively, the THz signal can be read via the same AA′ terminal via the magnetoresistance that originates from the oscillation of the $x$ component of the magnetization of the two sublattices [52].

## C. Systematic study for $\mathbf{p}_3$ spin polarization

Figures 4(a)–4(c) show the switching-on $J_{\mathrm{ON}}$ and switching-off $J_{\mathrm{OFF}}$ current density as a function of $d$, $\alpha$, and $A$ while maintaining the other two parameters constant. The threshold currents clearly increase with the increase of both the AFM thickness and the damping [Figs. 4(a) and 4(b)]. On the other hand, our simulations confirm that the exchange contribution plays an important role mainly in the switching-off current density, which slightly increases with the value of $A$, whereas the switching-on current density is almost constant
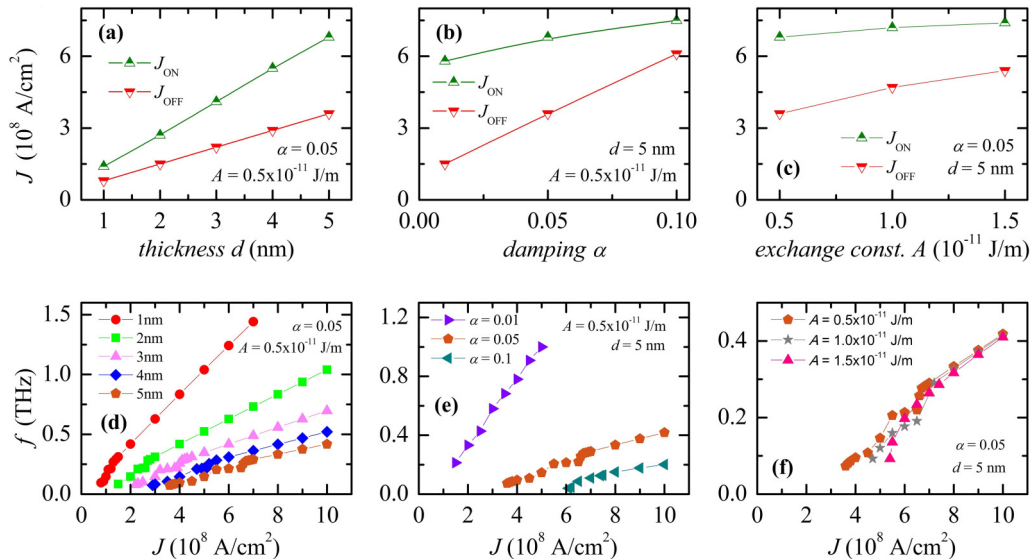


FIG. 4. Summary of micromagnetic simulations for a current applied along the $x$ axis, so that the spin Hall polarization is along the $y$ axis ($\theta_{\mathbf{p}} = 90°$). (a)–(c) Switching-on and -off current densities as a function of AFM thickness $d$ (a), damping $\alpha$ (b), and exchange constant $A$ (c). (d)–(f) Oscillation frequency of the $y$ component of the magnetization of the AFM as a function of the current density, for different values of the thickness $d$ (d), the damping $\alpha$ (e), and the exchange constant $A$ (f).
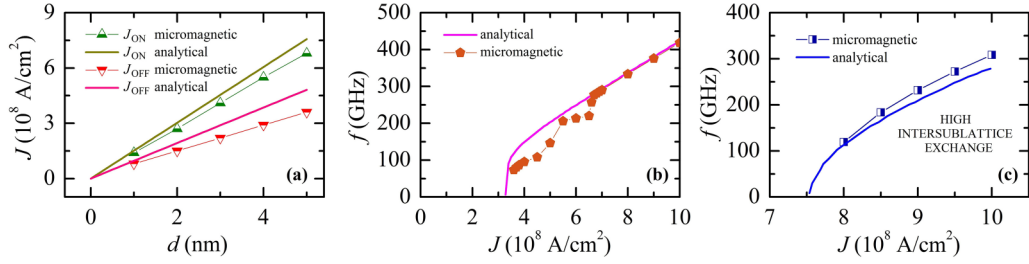
FIG. 5. Comparison between micromagnetic simulations and analytical models in the case $\theta_{\mathbf{p}} = 90°$: (a) threshold currents, (b) oscillation frequency of the $y$ component of the magnetization, and (c) oscillation frequency of the $y$ component of the magnetization in the case of high intersublattice exchange ($A_{\text{AFM}}/a^2 = 20 \text{ MJ/m}^3$).

[Fig. 4(c)]. The hysteresis width increases with the thickness, decreases with the damping, and slightly decreases with the value of $A$. Such results agree with the theoretical predictions (see Eqs. (4) and (5) of Ref. [32]).

Within the same parametric study, Figs. 4(d)–4(f) show the oscillation frequency (as computed from the $y$ component of the magnetization) of the excited dynamics as a function of the applied current $J$, for different values of thickness, damping, and exchange constant. The frequency tunability is blueshift on current with frequency values ranging from hundreds of gigahertz up to several terahertz. In particular, the frequencies increase with either the decrease of thickness [Fig. 4(d)] or damping [Fig. 4(e)]. In conclusion, full numerical micromagnetic simulations are in qualitative agreement with the theoretical predictions that hence can be used as a tool to identify the parameter region where to optimize the THz AFM-based oscillators [see Fig. 4(f), and Eqs. (6) and (7) of Ref. [32]].

The oscillation frequencies in Fig 4(e), computed for $a = 0.01$, shows a jump to zero at $J = 5 \times 10^8 \text{A/cm}^2$ where the dynamics of the $y$ component of the magnetization is off ($m_y$ is constant) and the trajectory is in the $x$-$z$ plane. This is a direct consequence of the reduced exchange stiffness or, in other words, the low thickness of the AFM film. As can be observed, the damping is a critical parameter either for the oscillation frequency or for the range of current tunability. This brings us to the conclusion that the THz dynamics in ultralow-damping AFMs will be observable in a narrow range of current density, at least if we read out the signal via the spin Hall resistance.

We have also performed simulations of a smaller ($30 \times 30 \text{ nm}^2$) and a larger ($80 \times 80 \text{ nm}^2$) AFM sample, with the default values for $d$, $A$, and $\alpha$, to reveal the possible role of the dimensions in the magnetization dynamics. However, those simulations have shown that both the current needed to switch on the dynamics and the frequency of oscillation turn out to be equal to the case of $40 \times 40 \text{ nm}^2$ sample. Actually, this outcome was expected, considering that the volume of the active layer does not appear in the analytical model.

### D. ASHO linewidth

Together with frequency tunability and threshold current, the linewidth is another fundamental property of an oscillator. In order to calculate the linewidth for the AFM oscillator, we have performed micromagnetic simulations at room temperature ($T = 300 \text{ K}$).

We have computed the linewidth for different values of current density, $T = 300 \text{ K}$, $\theta_{\mathbf{p}} = 90°$, and the default values for $d$, $\alpha$, and $A$. Our results point out that it is smaller than 10 MHz (our simulations are 100 ns long), corresponding to a quality factor of $Q = f/\Delta f = 41\,000$ at least.

### E. Comparison with analytical model

As already cited, our main numerical results agree with recently published theoretical predictions [32]. For this reason, we focused on a direct comparison between micromagnetic simulations and those analytical models, finding a good agreement for both the threshold currents and the output frequencies. Figure 5 summarizes this comparison. In the first graph, numerical threshold currents, as a function of the AFM layer thickness, are compared with the analytical formulas (Eqs. (4) and (5) in Ref. [32]):

$$
\begin{aligned}
J_{\text{ON}} &= \frac{\omega_{\text{ani}}}{2\sigma} \\
J_{\text{OFF}} &= \frac{2\alpha}{\pi\sigma}\sqrt{\omega_{\text{exch}}\omega_{\text{ani}}},
\end{aligned}
\tag{7}
$$

where $\omega_{\text{ani}} = \gamma_0(2K_U/M_S)$, $\sigma = (g\mu_B\theta_{SH}/2eM_Sd)$, $\omega_{\text{exch}} = \gamma_0(4A_{\text{AFM}}/a^2M_S)$.

Figure 5(b) shows the comparison concerning the output frequency of the oscillator for the default set of parameters. The analytical formula corresponds to Eq. (7) of Ref. [32]:

$$
\omega = \frac{\sigma J}{\alpha},
\tag{8}
$$

where, however, we are referring to the double frequency of the $y$ component of the magnetization.

We also performed numerical and analytical calculations in the case of higher exchange, considering $A_{\text{AFM}}/a^2 = 20 \text{MJ/m}^3$. Again, the comparison is convincing [see Fig. 5(c)], and we can state that, from the qualitative point of view, there is no significant change in the dynamics and in the inertial nature of their excitation.

### F. Effect of the DMI

The need of the full micromagnetic framework to analyze the magnetization dynamics in an AFM driven by SHE is clear in the presence of the interfacial DMI. The first effect of the interfacial DMI is on the ground state. In particular, Fig. 6 shows the evolution of the equilibrium configuration of the magnetization for different $D$. Starting from the uniform state [Fig. 6(a)], Néel-type domain walls (DWs) are stabilized
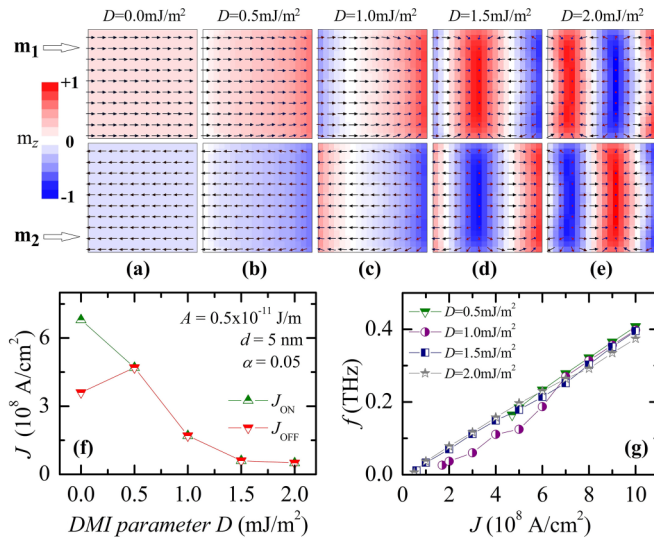
**(a)–(e)** FIG. 6. (a)–(e) Equilibrium configurations of the magnetization in the two sublattices as a function of the interfacial DMI parameter $D$. (f) Switching-on and -off current densities as a function of $D$. (g) Oscillation frequency of the spin Hall magnetoresistance as a function of current density for different values of $D$.



FIG. 7. (a) Equilibrium configuration of the magnetization in the two sublattices in the case of high interlayer exchange ($A_{\mathrm{AFM}}/a^2 = 20\,\mathrm{MJ/m^3}$) for $D = 1.5\,\mathrm{mJ/m^2}$. (b) Comparison of the output frequency with low and high intersublattice exchange for $D = 1.5\,\mathrm{mJ/m^2}$.

starting from $D = 1.5\,\mathrm{mJ/m^2}$ [see Figs. 6(c)–6(e)] [53–55]. The second effect is the change of the bifurcation at $D = 1.0\,\mathrm{mJ/m^2}$ from subcritical to supercritical and hence with the disappearing of the hysteretic excitation ($J_{\mathrm{ON}} = J_{\mathrm{OFF}}$) as displayed in Fig. 6(f). The third effect is the qualitative change of the magnetization dynamics that now it is characterized by a continuous nucleation, shifting, and annihilation of DWs along a direction that depends on the applied current (see Supplemental Material [48], Movies 1 and 2, to compare the dynamics at $D = 0.0\,\mathrm{mJ/m^2}$ and $2.0\,\mathrm{mJ/m^2}$) [56]. Figure 6(g) summarizes the output frequency as a function of current density for different DMI parameters and it turns out that DMI does not play a very important role in this case. This result is due to the fact that the main role of the DMI is the stabilization of the domain-wall chirality.

We performed micromagnetic simulations considering a high intersublattice exchange, also in the case of interfacial DMI. The magnetic configuration of the AFM sublattices is still characterized by nonuniform DWs, which translate along the current as in the case of low exchange [see Fig. 7(a)] with the equilibrium configuration of sublattices obtained

for $D = 2.0\,\mathrm{mJ/m^2}$. The high exchange, moreover, does not influence significantly the frequency of dynamics, as shown in Fig. 7(b). Nucleation and dynamics of DWs, in fact, are strictly connected with nonlocal terms. These contributions generally come from magnetostatic and nonhomogeneous exchange fields, including DMI. Intersublattice homogeneous exchange, instead, is a local term, due to the interaction of the magnetization of the two sublattices in the same cell.

## IV. CONCLUSIONS

AFM materials are promising for the realization of a compact submicrometer-scale THz oscillator tunable with a current in a wide range of frequency ranging from few hundreds of GHz up to 1–2 THz. Actually, this idea is still not demonstrated experimentally; this paper contributes to furnish a more detailed numerical understanding of the THz dynamics driven by spin Hall effect. We find that the macrospin-based theoretical model can be used for a qualitative study at very low DMI while a full micromagnetic approach is necessary in the presence of DMI, which is an energy contribution that arises in most of the experimental promising solutions for AFM-based oscillators.

[1] P. H. Siegel, IEEE Trans. Microwave Theory Tech. **50**, 910 (2002).

[2] B. Ferguson and X.-C. Zhang, Nat. Mater. **1**, 26 (2002).

[3] C. Kulesa, IEEE Trans. Terahertz Sci. Technol. **1**, 232 (2011).

[4] B. Fisher, M. Hoffmann, H. Helm, G. Modjesch, and P. U. Jepsen, Semicond. Sci. Technol. **20**, S246 (2005).

[5] M. C. Beard, G. M. Turner, and C. A. Schmuttenmaer, Phys. Med. Biol. **47**, 3841 (2002).

[6] J. F. Federici, B. Schulkin, F. Huang, D. Gary, R. Barat, F. Oliveira, and D. Zimdars, Semicond. Sci. Technol. **20**, S266 (2005).

[7] T. J. Yen, W. J. Padilla, N. Fang, D. C. Vier, D. R. Smith, J. B. Pendry, D. N. Basov, and X. Zhang, Science **303**, 1494 (2004).

[8] C. D. Stoik, M. J. Bohn, and J. L. Blackshire, Opt. Express **16**, 17039 (2008).

[9] M. Tonouchi, Nat. Photonics **1**, 97 (2007).

[10] W. Withayachumnankul, G. M. Png, and X. Yin, Proc. IEEE **95**, 1528 (2007).

[11] B. S. Williams, Nat. Photonics **1**, 517 (2007).

[12] E. Seok, D. Shim, C. Mao, R. Han, S. Sankaran, C. Cao, W. Knap, and K. K. O, IEEE J. Solid-State Circuits **45**, 1554 (2010).

[13] M. Tsoi, A. G. M. Jansen, J. Bass, W.-C. Chiang, M. Seck, V. Tsoi, and P. Wyder, Phys. Rev. Lett. **80**, 4281 (1998).

[14] W. H. Rippard, M. R. Pufall, S. Kaka, S. E. Russek, and T. J. Silva, Phys. Rev. Lett. **92**, 027201 (2004).

[15] V. Puliafito, B. Azzerboni, G. Consolo, G. Finocchio, L. Torres, and L. Lopez-Diaz, IEEE Trans. Magn. **44**, 2512 (2008).

[16] Z. Zeng, G. Finocchio, and H. Jiang, Nanoscale **5**, 2219 (2013).

[17] L. Zhang, B. Fang, J. Cai, M. Carpentieri, V. Puliafito, F. Garesci, P. Khalili Amiri, G. Finocchio, and Z. Zeng, Appl. Phys. Lett. **113**, 102401 (2018).

[18] V. Puliafito, A. Giordano, A. Laudani, F. Garescì, M. Carpentieri, B. Azzerboni, and G. Finocchio, Appl. Phys. Lett. **109**, 202402 (2016).

[19] L. Duo, M. Finazzi, and F. Ciccacci, *Magnetic Properties of Antiferromagnetic Oxide Materials: Surfaces, Interfaces, and Thin Films* (Wiley-VCH, Weinheim, 2010).

[20] V. Baltz, G. Gaudin, P. Somani, and B. Dieny, Appl. Phys. Lett. **96**, 262505 (2010).

[21] S.-H. Yang, K.-S. Ryu, and S. Parkin, Nat. Nanotechnol. **10**, 221 (2015).

[22] R. Tomasello, V. Puliafito, E. Martinez, A. Manchon, M. Ricci, M. Carpentieri, and G. Finocchio, J. Phys. D: Appl. Phys. **50**, 325302 (2017).

[23] O. Gomonay, K. Yamamoto, and J. Sinova, J. Phys. D: Appl. Phys. **51**, 264004 (2018).

[24] P. E. Roy, R. M. Otxoa, and J. Wunderlich, Phys. Rev. B **94**, 014439 (2016).

[25] K. Olejnik, V. Schuler, X. Marti, V. Novák, Z. Kaspar, P. Wadley, R. P. Campion, K. W. Edmonds, B. L. Gallagher, J. Garces, M. Baumgartner, P. Gambardella, and T. Jungwirth, Nat. Commun. **8**, 15434 (2017).

[26] A. S. Núñez, R. A. Duine, P. Haney, and A. H. MacDonald, Phys. Rev. B **73**, 214426 (2006).

[27] T. Moriyama, N. Matsuzaki, K.-J. Kim, I. Suzuki, T. Taniyama, and T. Ono, Appl. Phys. Lett. **107**, 122403 (2015).

[28] L. Liu, T. Moriyama, D. C. Ralph, and R. A. Buhrman, Phys. Rev. Lett. **106**, 036601 (2011).

[29] E. V. Gomonay and V. M. Loktev, Low Temp. Phys. **40**, 17 (2014).

[30] R. Cheng, D. Xiao, and A. Brataas, Phys. Rev. Lett. **116**, 207603 (2016).

[31] S. Baierl, J. H. Mentink, M. Hohenleutner, L. Braun, T.-M. Do, C. Lange, A. Sell, M. Fiebig, G. Woltersdorf, T. Kampfrath, and R. Huber, Phys. Rev. Lett. **117**, 197201 (2016).

[32] R. Khymyn, I. Lisenkov, V. Tiberkevich, B. A. Ivanov, and A. Slavin, Sci. Rep. **7**, 43705 (2017).

[33] V. Baltz, A. Manchon, M. Tsoi, T. Moriyama, T. Ono, and Y. Tserkovnyak, Rev. Mod. Phys. **90**, 015005 (2018).

[34] O. Gomonay, V. Baltz, A. Brataas, and Y. Tserkovnyak, Nat. Phys. **14**, 213 (2018).

[35] M. B. Jungfleish, W. Zhang, and A. Hoffmann, Phys. Lett. A **382**, 865 (2018).

[36] A. Manchon, I. M. Miron, T. Jungwirth, J. Sinova, J. Zelezný, A. Thiaville, K. Garello, and P. Gambardella, arXiv:1801.09636 (2018).

[37] N. Ntallis and K. G. Efthimiadis, Compt. Mater. Sci. **97**, 42 (2015).

[38] A. Fert, and P. M. Levy, Phys. Rev. Lett. **44**, 1538 (1980).

[39] Y. A. Kuznetsov, *Elements of Applied Bifurcation Theory*, 2nd ed. (Springer, New York, 1998).

[40] D. Suess, T. Schrefl, W. Scholz, J.-V. Kim, R. L. Stamps, and J. Fidler, IEEE Trans. Magn. **38**, 2397 (2002).

[41] https://www.ctcms.nist.gov/~rdm/org.html (problem 4, specifications).

[42] A. A. Sapozhnik, R. Abrudan, Y. Skourski, M. Jourdan, H. Zabel, M. Kläui, and H.-J. Elmers, Phys. Status Solidi **11**, 1600438 (2017).

[43] G. Finocchio, B. Azzerboni, G. D. Fuchs, R. A. Buhrman, and L. Torres, J. Appl. Phys. **101**, 063914 (2007).

[44] G. Finocchio, I. N. Krivorotov, X. Cheng, L. Torres, and B. Azzerboni, Phys. Rev. B **83**, 134402 (2011).

[45] M. d'Aquino, C. Serpico, R. Bonin, G. Bertotti, and I. D. Mayergoyz, Phys. Rev. B **84**, 214415 (2011).

[46] G. Finocchio, V. Puliafito, S. Komineas, L. Torres, O. Ozatay, T. Hauet, and B. Azzerboni, J. Appl. Phys. **114**, 163908 (2013).

[47] V. Puliafito, Y. Pogoryelov, B. Azzerboni, J. Akerman, and G. Finocchio, IEEE Trans. Nanotechnol. **13**, 532 (2014).

[48] See Supplemental Material at http://link.aps.org/supplemental/10.1103/PhysRevB.99.024405 for more information about the inertial nature of the antiferromagnetic oscillator, the double frequency of the component of the magnetization along the spin polarization, and for the movies described in the text.

[49] O. R. Sulymenko, O. V. Prokopenko, V. S. Tiberkevich, A. N. Slavin, B. A. Ivanov, and R. S. Khymyn, Phys. Rev. Appl. **8**, 064007 (2017).

[50] J. Sinova, S. O. Valenzuela, J. Wunderlich, C. H. Back, and T. Jungwirth, Rev. Mod. Phys. **87**, 1213 (2015).

[51] T. Moriyama, K. Oda, T. Ohkochi, M. Kimata, and T. Ono, Sci. Rep. **8**, 14167 (2018).

[52] S. Yu. Bodnar, L. Smeikal, I. Turek, T. Jungwirth, O. Gomonay, J. Sinova, A. A. Sapozhnik, H.-J. Elmers, M. Kläui, and M. Jourdan, Nat. Commun. **9**, 348 (2018).

[53] S. Emori, U. Bauer, S.-M. Ahn, E. Martinez, and G. S. D. Beach, Nat. Mater. **12**, 611 (2013).

[54] G. Siracusano, R. Tomasello, A. Giordano, V. Puliafito, B. Azzerboni, O. Ozatay, M. Carpentieri, and G. Finocchio, Phys. Rev. Lett. **117**, 087204 (2016).

[55] V. Puliafito, A. Giordano, B. Azzerboni, and G. Finocchio, J. Phys. D: Appl. Phys. **49**, 145001 (2016).

[56] M. Cubukcu, J. Sampaio, K. Bouzehouane, D. Apalkov, A. V. Khvalkovskiy, V. Cros, and N. Reyren, Phys. Rev. B **93**, 020401 (2016).